Model based control of a mock circulatory system for left ventricular assist device evalution

Vaes, M.H.E.

Award date:
2007

Model based control of a mock circulatory system for left ventricular assist device evaluation

M.H.E. Vaes

DCT 2007.85

Master's thesis

Engineering Thesis Committee:

prof. dr. ir. M. Steinbuch (DCT)
dr. ir. M.C.M. Rutten (BMT)
dr. ir. M.J.G. van de Molengraft (DCT)
dr. ir. P.H.M. Bovendeerd (BMT)

Eindhoven University of Technology

Department of Mechanical Engineering
Control Systems Technology Group

Department of Biomedical Engineering
Cardiovascular Biomechanics Group

Eindhoven, July, 2007

Abstract

Mock circulatory systems (MCS) are an important tool for the evaluation of the function and the assist properties of left-ventricular assist devices (LVADs). A new control strategy for a MCS has been developed with a more adaptive cardiac function described by the single fiber model of Arts et al. [1], and a baroreflex response to mimic the pressure-dependency of the heart rate. The control strategy is implemented using a pressure feedback control system. A reference left ventricular pressure is calculated by the heart model using left ventricular volume. The feedback controller regulates the left ventricular pressure according to this reference signal. Simulations and experiments on the MCS showed that the system responds to changes in afterload, preload and heart rate consistent with physiological observations. Implementation of a LVAD in the MCS showed that the system responds stable and robust to the introduction of cardiac assist devices. Since the single fiber holds several parameters to change the properties of the heart, like speed of contraction and wall volume, the control strategy can mimic various pathological conditions which can be used in the evaluation of LVADs.

Contents

1 Introduction

About 5 million Americans suffer from congestive heart failure (CHF) and each year 550,000 patients are newly diagnosed. Heart failure causes 57 thousand deaths each year in the US and takes more than 270 thousand lives as an underlying or contributing cause [2]. The best solution for end-stage patients, a heart transplant, is limited by an insufficient number of donors, as only 3000 donor organs are available worldwide per year [3]. An alternative treatment is the implementation of a left ventricular assist device (LVAD). A LVAD is a surgically implanted mechanical device that helps the heart pumping blood, thereby unloading the heart and restoring the blood flow to the circulation.
Several research tools are used to evaluate the functionality of LVADs. Mock circulatory systems (MCS) may be preferred as animal testing [4] and use in humans [5, 6] are limited in their ethical requirements. Another advantage of a MCS is the ability to evaluate LVADs under a wide variety of operating conditions, which would not be possible with a few in vivo trials. In other words, a MCS that responds to changes in preload and afterload of the heart and the capability of mimicking different pathological conditions, is an important tool for the evaluation of LVADs.
The ability to reproduce changes in ventricular function in response to changes in load is also known as the Frank-Starling response. Although most systems fail to reproduce the heart's Frank-Starling response [7, 8, 9, 10, 11], several attempts have been reported in literature to include this behaviour. Pantalos et al. [12], Timms et al. [13] and Gwak et al. [14] developed an artificial ventricle that mimics the Frank-Starling response. Their model ventricle consists of a flexing, segmented sac inside a pressurization chamber. The contraction of the ventricle is controlled by pressurizing the chamber during systole, and releasing the it during diastole. The rate of in and outflow of the compressed air determines the heart rate.
A more widely used approach is the use of a time-varying elastance model to reproduce the cardiac function of the heart. It describes the contraction of the ventricle over the cardiac cycle with an elastance that varies in time [15]. Ferrari et al. [16, 17, 18, 19, 20, 21], Baloa et al. [22] and Colacino et al. [23] created mock circulatory systems that include cardiac function based upon a supplied time-varying elastance, and work at a preset, constant heart rate. However, Vandenberghe et al. [24] recently stated that the time-varying elastance insufficiently models the hemodynamics of a mechanically assisted left ventricle, due to the static nature of the elastance curve. Therefore, a heart model should be used which incorporates ejection rate dependence behaviour of the muscle fiber. So far, this behaviour has only been included by Ferrari et al. , who used a corrective function for the time-varying elastance [25], taking into account ejection rate and ejection volume.
In this study, a heart model will be used in which the ejection rate dependence is already a part of the cardiac description rather than correcting an existing cardiac function. This heart model consists of two parts. The myocardial mechanical material properties will be phenomenologically modelled with the Hill-type model [26], describing the active and passive behaviour of the myocardial material. The cardiac geometrical properties are modelled with the single-fiber model of Arts et al. [1]. The single-fiber model has some useful advantages compared to the time-varying elastance model. It holds several parameters to adjust

the properties of the pathologic heart, like the speed of contraction. Furthermore, the single-fiber model includes damping as well, as the model is sensitive to rate of volume change, thereby increasing the stability of the whole system.
Another limitation of current mock circulatory systems is that they all operate on a fixed frequency. In these systems, the heart frequency does not change in response to changes in the loading of heart. Although heart rate variation is the most important factor in cardiac output regulation [27]. In this study, a baroreflex model proposed by van Roon et al. [28] will be added to the control strategy to regulate the frequency of the heart.
The aim of this study is to design and control a MCS using the single-fiber model and a baroreflex response. The control strategy is implemented using a pressure feedback control system. A reference left ventricular pressure is calculated by the heart model using left ventricular volume. The pressure feedback controller regulates the left ventricular pressure according to this reference signal. The control algorithm should respond stable and robust to changes in load and heart frequency. The algorithm should also be able to simulate normal conditions and allow the introduction of a LVAD. The control strategy will be designed for an improved version of the mock circulatory system proposed by Geven et al. [29]. A servo controller will be designed by manual loop shaping using frequency response function (FRF) measurements [30]. In this study a mathematical model will be given that describes the MCS numerically. The model will be used to evaluate the control strategy and to compare the results with those from the MCS. The paper concludes with a discussion about the main features and limitations of the control strategy and how the system can be used to evaluate LVADs.

2 Material and Methods

2.1 Mock circulatory system

The mock circulatory system used in this study is based on the system as described by Geven et al. [29]. The system designed by Geven consists of three parts: a left ventricle, a systemic circulation and a coronary circulation. For this study, the coronary circulation is neglected. The left ventricle includes a piston-pump and two tri-leaflet polyurethane valves (Hemolab, the Netherlands). The afterload consists of a flexible tube (Hemolab, the Netherlands) connected to a four-element windkessel [31]. Two external occluders regulate systemic and peripheral resistance. In the setup, left ventricular volume V_{lv}, left ventricle pressure p_{lv}, aortic flow q_{ao} and aortic pressure p_{ao} are measured continuously. The system is extended with a preload, modelling the venous return to the left heart. The preload consists of a windkessel between the peripheral resistance and the mitral valve (figure 1).

2.2 Mathematical model

The mathematical description of the setup is divided into three parts, the hemodynamic preload and afterload, the piston pump and the heart valves (figure 2). The hemodynamic preload and afterload are described with a lumped parameter model [31]. The pump is modelled as a pressure source, generating

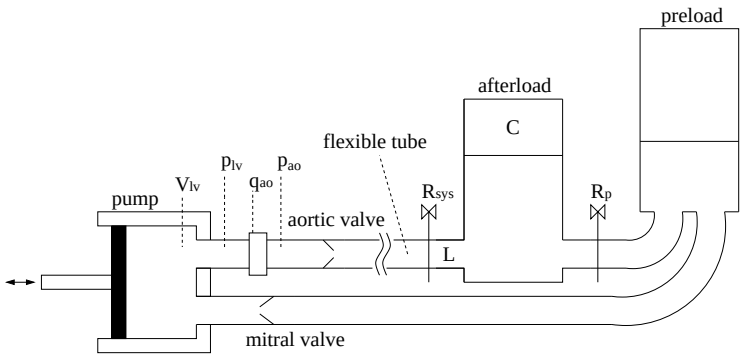

Figure 1: Schematic of the mock circulatory system

a pressure p_p depending on the piston position x and the two flows q_{mv} and q_{ao}. Due to its design, the pump also has a small compliance C_p: The piston is modelled as a mass m with damping d for the friction between the piston and the pump housing. Combination of pump, piston and hemodynamic preload and afterload, results in a seventh order system of differential equations:

$$\frac{\partial x}{\partial t} = v, \tag{1}$$

$$\frac{\partial v}{\partial t} = -\frac{d}{m}v + \frac{k}{m}u, \tag{2}$$

$$\frac{\partial p_p}{\partial t} = \frac{1}{C_p}q_p = \frac{1}{C_p}\left(A_z v + q_{mv} - q_{av}\right), \tag{3}$$

$$\frac{\partial p_1}{\partial t} = R_{art}\frac{\partial q_{ao}}{\partial t} + \frac{\partial p_{art}}{\partial t}, \tag{4}$$

$$\frac{\partial p_2}{\partial t} = -R_{ven}\frac{\partial q_{mv}}{\partial t} + \frac{\partial p_{ven}}{\partial t}, \tag{5}$$

$$\frac{\partial p_{art}}{\partial t} = \frac{1}{C_{art}}q_{ao} + \frac{1}{C_{art}R_p}(p_{ven} - p_{art}), \tag{6}$$

$$\frac{\partial p_{ven}}{\partial t} = -\frac{1}{C_{ven}}q_{mv} + \frac{1}{C_{art}R_p}(p_{art} - p_{ven}) \tag{7}$$

with x the piston position, v the piston velocity, u the input voltage. The relations for the aortic pressure p_{ao} and vena cava pressure p_{vc} are:

$$p_{ao} = p_1 + L_{art}\frac{\partial q_{ao}}{\partial t}, \tag{8}$$

$$p_{vc} = p_2 + L_{ven}\frac{\partial q_{mv}}{\partial t}. \tag{9}$$

The valves are modelled as short tubes with length l in which flow is dominated by inertia. The sum of the effects of inertia due to acceleration in time and the Bernoulli effect, yields an expression for the time derivative of the flow [32]:

$$\frac{\partial q}{\partial t} = \frac{1}{\rho l}\left(\Delta p A - \frac{\rho q^2}{2A}\right) \tag{10}$$

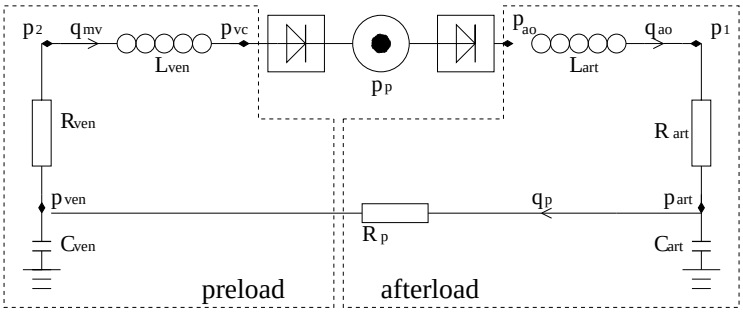

Figure 2: Schematic representation of the systemic circulation

with ρ the medium density and A the cross-sectional area of the valve. Opening and closing of the valves is modelled by instantaneous changes in the cross-sectional area, and depends on the direction of the flow q and the pressure difference Δp.

$$A = c \cdot A_{open} + (1 - c) \cdot A_{leak} \tag{11}$$

$$c = \begin{cases} 0 & q < 0 \vee \Delta p < 0 \\ 1 & q > 0 \vee \Delta p > 0 \end{cases} \tag{12}$$

with A_{open} and A_{leak} the given valve cross-sectional areas of the open and closed valve, respectively. The leak area is used to prevent singularities in the set of equations. The values of the parameters are listed in table 1.

2.2.1 Single Fiber Model

Arts et al. [1] derived a relation between the cavity pressure and volume and the myocardial fiber stress and strain. This relationship assumes that muscle fiber stress and strain are homogeneously distributed in the normal left ventricle. Myofiber stress and strain may therefore be approximated by single values, being valid for the whole wall.
The myofiber stress σ_f is modelled as a function of sarcomere length l_s with the Hill-type model [26]. This model consists of a passive elastic component in parallel with a contractile element. The passive elastic component describes the behaviour of the passive muscle. The contractile element describes the additional stress due to muscle activation, depending on sarcomere length l_s, sarcomere shortening velocity v_s and time t. The fiber stress is a summation of passive stress σ_{pas} and active stress σ_{act}.

$$\sigma_f = \sigma_{pas}(l_s) + \sigma_{act}(l_s, v_s, t) \tag{13}$$

with

$$\sigma_{pas} = \sigma_{pas0} \exp(c_p(l_s - l_{sp0}) - 1) \tag{14}$$

$$\sigma_{act}(l_s, t_a, v_s) = f(l_s)g(t_a)h(v_s) \tag{15}$$

The functions $f(l_s)$, $g(t_a)$ and $h(v_s)$ are modelled to fit experimental data from Kentish et al. [33] and Janssen et al. [34].

$$f(l_s) = \begin{cases} 0 & l_s \leq l_{sa0} \\ \sigma_{ao} \left(\frac{l_s}{l_{sa0}} - 1 \right)^c & l_s > l_{sa0} \end{cases}$$

$$g(t_{t_a}) = \begin{cases} 0 & t_a < 0 \\ sin^2\left(\frac{\pi}{2}\frac{t_a}{\tau_r} - 1\right) & 0 \le t_a \le \tau_r \\ 1 - sin^2\left(\frac{\pi}{2}\frac{t_a - \tau_r}{\tau_d} - 1\right) & \tau_r \le t_a \le \tau_d + \tau_r \\ 0 & t_a > \tau_r + \tau_d \end{cases} \quad (16)$$

with

$$\tau_r = \tau_{r0}(1 + a_r(l_s - l_{a0})) \quad (17)$$

$$\tau_d = \tau_{d0}(1 + a_d(l_s - l_{a0})) \quad (18)$$

$$h(v_s) = \frac{1 - (v_s/v_0)}{1 + a(v_s/v_0)} \quad (19)$$

with

$$v_s(t) = -dl_s/dt \quad (20)$$

Assuming rotational symmetry and homogeneity of mechanical load in the wall, gives a relation between myofiber stress and left-ventricular pressure:

$$\frac{\sigma_f}{p_{lv}} = \left(1 + 3\frac{V_{lv}}{V_w}\right). \quad (21)$$

Equation (21) shows that wall stress increases with cavity volume for a given pressure. Conservation of energy yields a relation between ventricular volume and sarcomere length, with incremental pump work equal to the incremental work generated by the myofibers

$$p_{lv} dV_{lv} = V_w \frac{\sigma_f}{l_s} dl_s. \quad (22)$$

Substituting equation (21) into equation (22) yields

$$\frac{l_s}{l_{s0}} = \left(\frac{1 + 3\frac{V_{lv}}{V_w}}{1 + 3\frac{V_{lv0}}{V_w}}\right)^{\frac{1}{3}}, \quad (23)$$

with l_{s0} the sarcomere length and V_{lv0} the cavity volume in the reference state.

2.2.2 Baroreflex model

The heart rate control model in this study is based on the baroreflex model, as presented by van Roon et al. [28]. The baroreflex is mainly involved in short-term systemic pressure control. Changes in systemic pressure are registered by the baroreceptors that signal these changes to the brain, resulting in vagal and sympathetic nervous responses adjusting the heart rate.
The baroreflex models the heart rate as a function of mean systemic pressure using a function that starts to rise above 50 mmHg and saturates above 180 mmHg (figure 3, left). The response time of the baroreflex system is typically tens of seconds (figure 3, right).

2.2.3 Parameter Estimation

The hemodynamic parameters are derived from Fourier analysis on the measured aortic pressure and aortic flow. A Fourier transformation yields the pressure and flow harmonics, after which a least squares estimation provides the

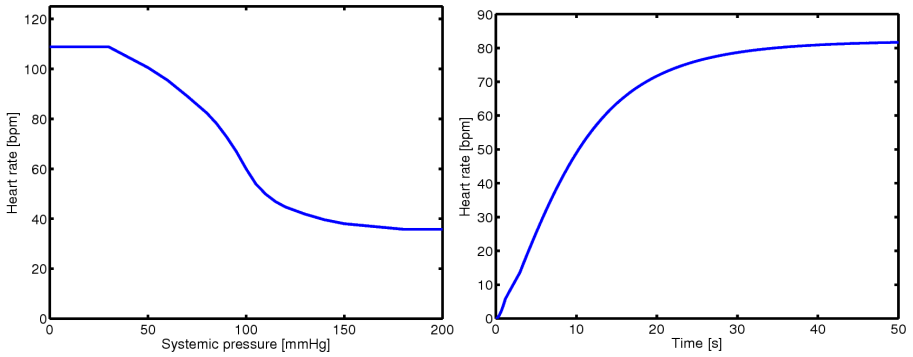

Figure 3: Baroreflex function; left panel shows the pressure-frequency response, right panel shows a 80 mmHg pressure step response

hemodynamic parameters. A description on how the pump compliance has been computed is given in Appendix D. The heart valve areas are adapted from van Gerven et al. [35]. The parameters for the single fiber model are derived from literature [33, 34]. Piston mass m, area A_z and length L_0 were measured. A complete overview of all parameters is given in table 1.

2.3 Controller Design

A common method in linear control theory for the design of a servo controller, is manual loop shaping of the open loop frequency response function (FRF) of the system [30]. A FRF measurement of the system has been acquired with the sensitivity method, the most common method for FRF measurements in closed loop. This method measures the input voltage to the system $u(t)$ and an excited extra input $w(t)$ to determine an estimation of the sensitivity function $S(\jmath\omega)$ of the system. The sensitivity function is used to calculate the FRF which is used for the controller design.
The three goals in the design of the servo controller were stability, robustness and disturbance attenuation. The tracking error should be minimized while preserving stability and robustness in a wide variety of conditions. The designed controller consists of three components. A lead compensator has been used for phase advance in the resonance frequency region to increase the robustness. A integral action is used for disturbance rejection at low frequencies. A second order low-pass filter takes care of measurement noise reduction and robustness at high frequencies. The open loop transfer function now has a bandwidth of 40 Hz (figure 4). The open loop Nyquist plot (figure 4), a plot of frequency response function in the complex plane, shows stability and robustness of the controlled system, as it passes the point (-1,0) with a sufficient margin.
A feedforward controller has been added to improve the performance of the system (figure 6). The feedforward controller is based on the inverse of the model described by (1) and (2). The pressure trajectory, generated by the single-fiber model, is used as the input for the feedforward, the output signal is added to the servo controller. The controller now tracks the pressure trajectory (figure 5) with error margins smaller than 22 mmHg and an average value of 3.2 mmHg. These peak errors of 22 mmHg are caused by the closure of the

Table 1: Table of the measured and estimated parameters

Name	Symbol	Value	Units
Arterial inertance	L_{art}	$3.14 \cdot 10^{5}$	$Pa \cdot s^2 \cdot m^{-3}$
Arterial compliance	C_{art}	$1.90 \cdot 10^{-8}$	$m^3 \cdot Pa^{-1}$
Arterial resistance	R_{art}	$1.95 \cdot 10^{8}$	$Pa \cdot s \cdot m^{-3}$
Peripheral resistance	R_p	$2.52 \cdot 10^{7}$	$Pa \cdot s \cdot m^{-3}$
Venous inertance	L_{ven}	$7.03 \cdot 10^{3}$	$Pa \cdot s^2 \cdot m^{-3}$
Venous compliance	C_{ven}	$3.15 \cdot 10^{-5}$	$m^3 \cdot Pa^{-1}$
Venous resistance	R_{ven}	$3.73 \cdot 10^{6}$	$Pa \cdot s \cdot m^{-3}$
Pump compliance	C_p	$5.09 \cdot 10^{-10}$	$m^3 \cdot Pa^{-1}$
Piston area	A_z	$2.28 \cdot 10^{-3}$	m^2
Piston mass	m	0.12	kg
Piston damping	d	12	$kg \cdot s^{-1}$
Piston length	L_0	0.045	m
Aortic valve length	l_{av}	$2.1 \cdot 10^{-2}$	m
Mitral valve length	l_{mv}	$2.7 \cdot 10^{-2}$	m
Aortic valve area	$A_{open,av}$	$4.5 \cdot 10^{-4}$	m^2
Aortic valve area	$A_{leak,av}$	$4.5 \cdot 10^{-8}$	m^2
Mitral valve area	$A_{open,mv}$	$7.2 \cdot 10^{-4}$	m^2
Mitral valve area	$A_{leak,mv}$	$7.2 \cdot 10^{-8}$	m^2
Medium density	ρ	$1.05 \cdot 10^{3}$	$kg \cdot m^{-3}$
Scaling parameter for active stress	σ_{a0}	$180 \cdot 10^{3}$	Pa
Curvature of stress-length relation	c	1.0	-
Sarcomere length with zero stress	l_{sa0}	$1.6 \cdot 10^{-6}$	m
Rise time active stress for $l_s = l_{a0}$	τ_{r0}	$50 \cdot 10^{-3}$	s
Length dependence of rise time	a_r	$150 \cdot 10^{3}$	$s \cdot m^{-1}$
Decay time active stress for $l_s = l_{a0}$	τ_{d0}	$100 \cdot 10^{-3}$	s
Length dependence of decay time	a_d	$300 \cdot 10^{3}$	$s \cdot m^{-1}$
Unloaded shortening velocity	v_0	$0.01 \cdot 10^{-3}$	$m \cdot s^{-1}$
Curvature of stress-velocity relation	a	2.0	-
Scaling parameter for passive stress	σ_{pas0}	$0.9 \cdot 10^{3}$	Pa
Curvature passive stress relation	c_p	$6 \cdot 10^{6}$	m^{-1}
Reference sarcomere length	l_{sp0}	$2.0 \cdot 10^{-6}$	m
Left ventricle wall volume	V_w	$200 \cdot 10^{-6}$	m^3
Left ventricular reference cavity volume	V_{lv0}	$66.7 \cdot 10^{-6}$	m^3
Reference sarcomere length	l_{s0}	$2.0 \cdot 10^{-6}$	m

mitral valve. During the rest of the trajectory the error is considerably smaller with values below 10 mmHg. A detailed explanation of the controller design is described in appendix E.

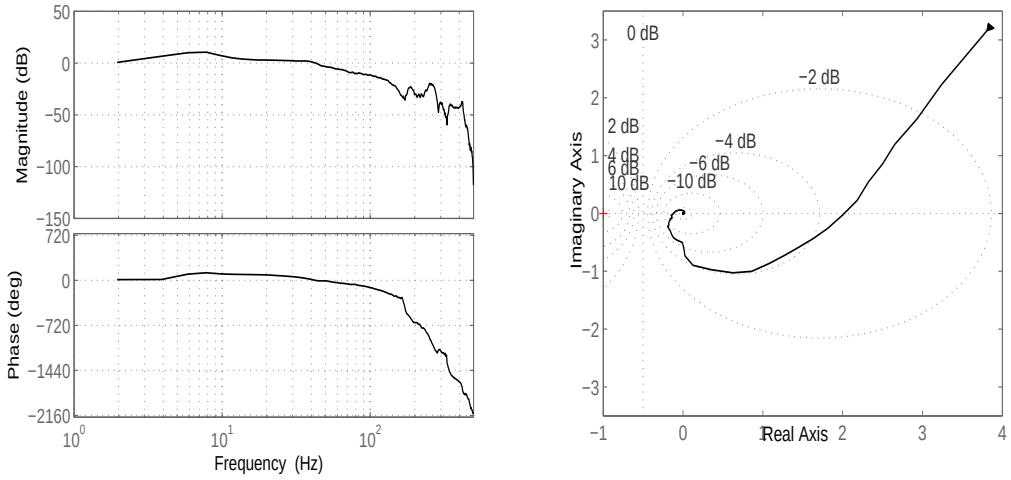

Figure 4: Left panel shows the open loop frequency response, the right panel shows the Nyquist plot of the open loop response

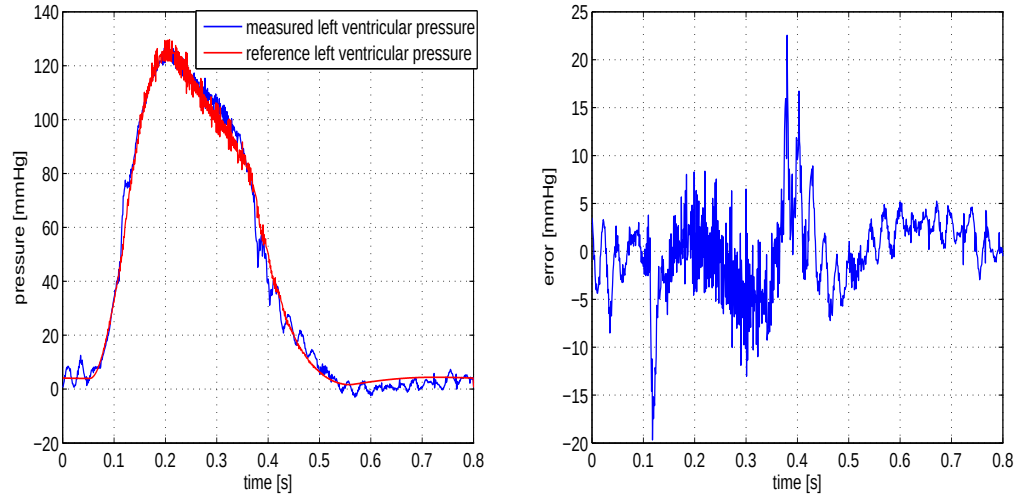

Figure 5: Left panel shows the reference and measured left ventricular pressure. The right panel shows error signal between reference and tracked pressure signal.

2.4 Hardware Implementation

Data acquisition and control of the servo drive is performed with Matlab/Simulink software and a TUeDACS QAD, a data acquisition and control system developed at the Eindhoven University of Technology [36]. The system is connected to a servo drive (BLH30, Parker) and a servomotor (ML2340, Parker) with a linear actuator (ETB32, Parker). Piston position is measured with quadrature encoders, with a resolution of 2000 pulses per revolution, which corresponds to 200 pulses per millimeter stroke. Pressure sensors (P10EZ-1, Becton Dickinson) are used to measure pump and aortic pressure. Aortic flow is measured with a flow probe (28PAX, Transonic) connected to a flow meter (TS420, Transonic). Figure 6 shows a block diagram of the control loop. The heartmodel-block, containing the single-fiber model, receives the measured left-ventricular volume as input and calculates a desired left-ventricular pressure. This value is compared with the pump pressure measured at the setup. The controller-block contains the designed servo controller and calculates a control signal that is sent to the servo drive. The control loop is operated at a 1 kHz update rate.

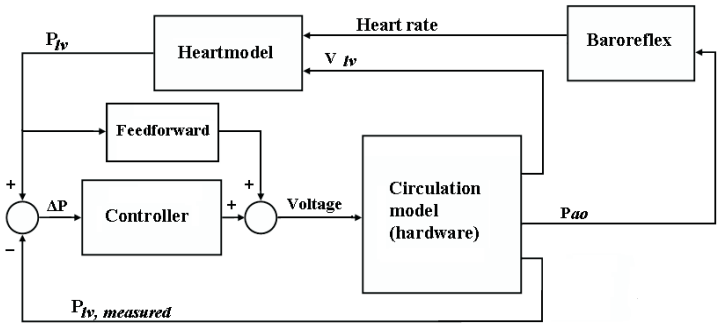

Figure 6: Schematic block diagram of the control scheme used in Simulink

2.5 Protocol

Results have been obtained to verify the ability of the MCS to reproduce the hemodynamic characteristics of the human circulatory system. During the experiments, left ventricular pressure and volume, and aortic pressure and flow are measured.

First, experiments have been conducted by varying preload and afterload at a constant heart rate of 75 beats per minute (bpm). Preload was varied by adjusting the venous compliance, causing a change in end-diastolic volume. Afterload is varied by adjusting the peripheral resistance, thereby changing the systolic pressure. At the same time, preload was held constant by adjusting the venous compliance. The unfiltered pressure, flow and volume data from the experiments were used to calculate hemodynamic parameters, with all beats averaged to obtain a single mean value for each parameter. The characterizing hemodynamic parameters were used in simulations to acquire numerical data as well.

Second, heart rate was varied to prove robustness of the designed servo controller and to show the ability of the setup to operate on different heart rates. The rate was increased with steps of 30 bpm in a range between 45 bpm and 135 bpm. A pressure volume loop was measured using the acquired data and the passive stress line was added to show the adherence of the control strategy to the single fiber model.
The baroreflex model was used in the third experiment to control the heart rate. The experiments have been conducted to show the response of the baroreflex control model to a variation of the preload.
A pneumatically driven LVAD (PVAD, Thoratec) was connected to the mock system in the final experiment. The LVAD was connected between the left ventricle and the aorta. A Hall sensor in the LVAD detects when the device is completely filled and triggers the ejection of the LVAD. With a second flow probe it was now possible to measure before (aortic flow) and after (total flow) the point where the LVAD was connected to the setup.
All data were filtered offline using a 4th order zero phase forward and reverse digital filter at a cut-off frequency of 50Hz. Pressure-volume (pV) loops were constructed by plotting left-ventricular pressure against left-ventricular volume. A passive stress line, described by the single fiber model during the filling of the ventricle, is added to the pV loops to show that the control strategy follows the single fiber model.

3 Results

Varying the preload at a constant heart rate results in the pressure volume loops as depicted in figure 7. A regression line through the points with the highest pressure-volume ratio was added to the figure. The coefficients of the regression line are found by a least-squares estimate of these points. The slope of the regression line was found to be 0.80 in both the numerical and experimental case.

Figure 8 depicts the pressure-volume loops for three different afterload settings. The afterload was varied by adjusting the peripheral resistance, thereby raising the systolic pressure. Again a regression line of the points with the highest pressure-volume ratio has been added. The result shows that the control strategy is not sensitive to changing afterloads, as the slope of the regression line is maintained. Figure 8 also shows that the increase in afterload and hence increase in aortic pressure, results in a decrease in stroke volume. Also in this case, the pressure-volume loop follows the passive stress described by the single fiber model (indicated by the dotted passive stress line) during the filling of the ventricle.
The left panel of figure 9 shows the result of a variation in rates over a range from 45 bpm to 135 bpm. The dotted line proves that the pV-loops follow the passive stress during the filling phase for all heart rates that were used in the experiments
Next the baroreflex model was used to control the heart rate. The right panel of figure 9 shows the result of a sudden increase of the preload after 10 seconds. Left ventricular pressure and end-diastolic volume respond to the preload change, similar to the results of figure 7. However, the heart rate does not remain constant now, but is decreased by the baroreflex mechanism as a result of

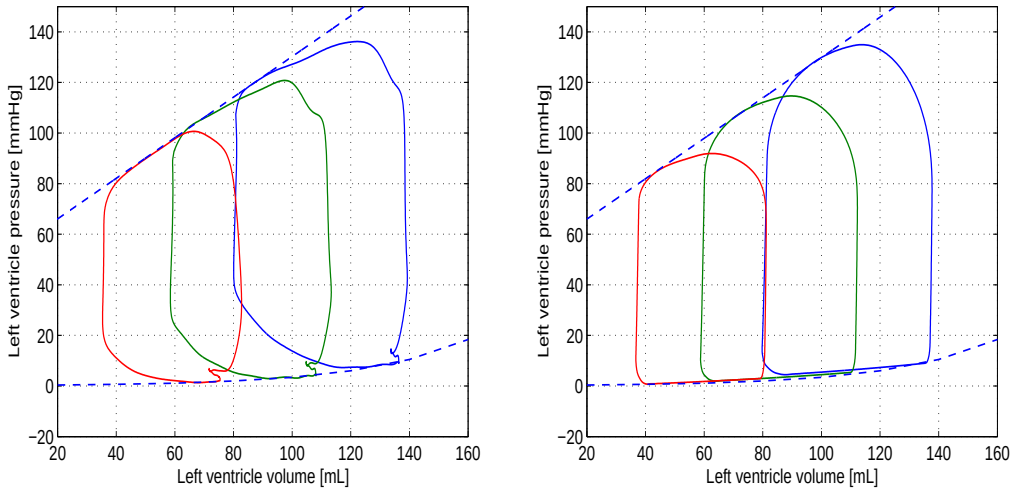

Figure 7: pV loop for varying preloads. The left panel shows the experimental results, the right panel shows the results of the numerical model

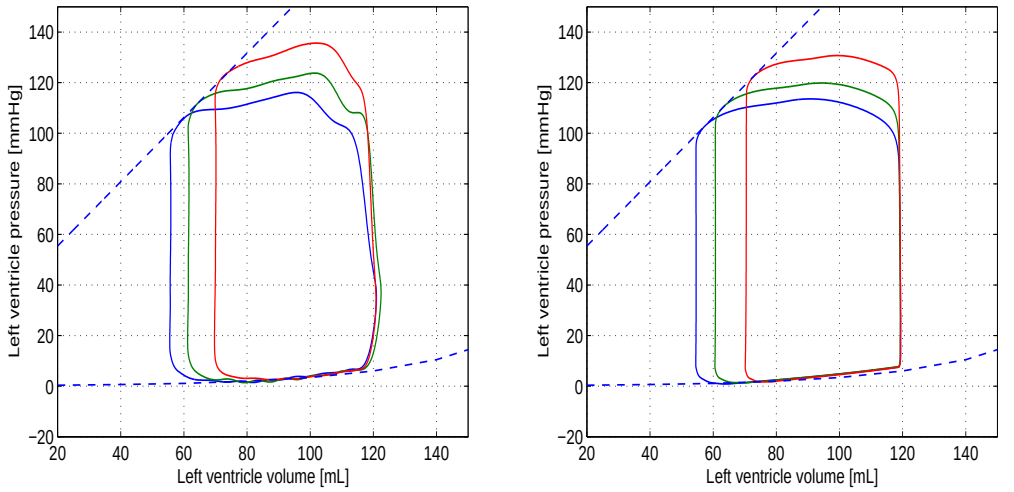

Figure 8: pV loop for various afterloads. The left panel shows the experimental results, the right panel shows the results of the numerical model

the preload change.
Figure 10 depicts the result of the experiments with the LVAD. The upper graph shows the aortic flow (dashed line) and the total flow (solid line) and the middle graph depicts the pressure in the left-ventricle (solid line) and aortic pressure (dashed line). The pV loops of the experiment are shown in the lower graph of

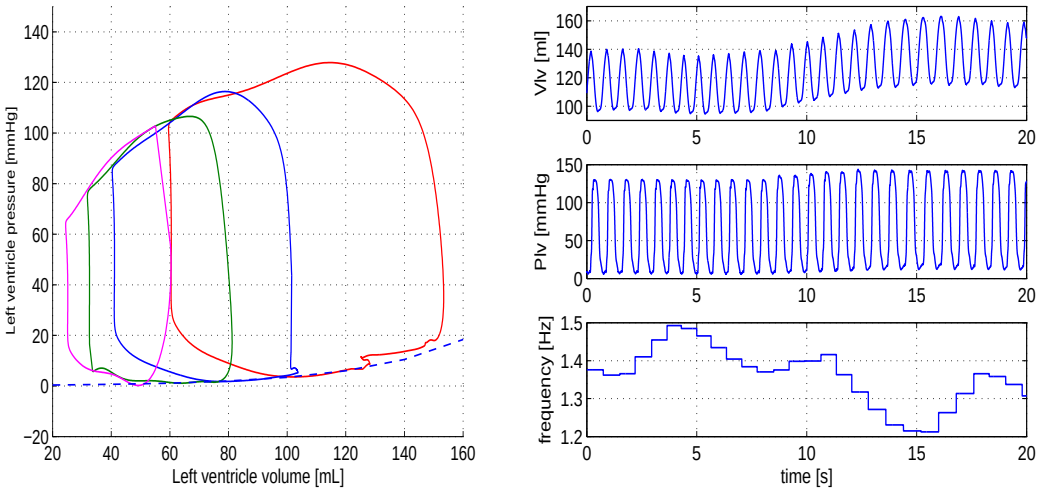

Figure 9: Left panel: PV loops for heart rates of 135 bpm, 105 bpm, 75bpm and 45 bpm Hz (from left to right). Right panel: Response of left ventricular volume (upper panel), left ventricular pressure (middle panel) and heart rate (lower panel) to changing heart rates, controlled by the baroreflex mechanism.

figure 10.

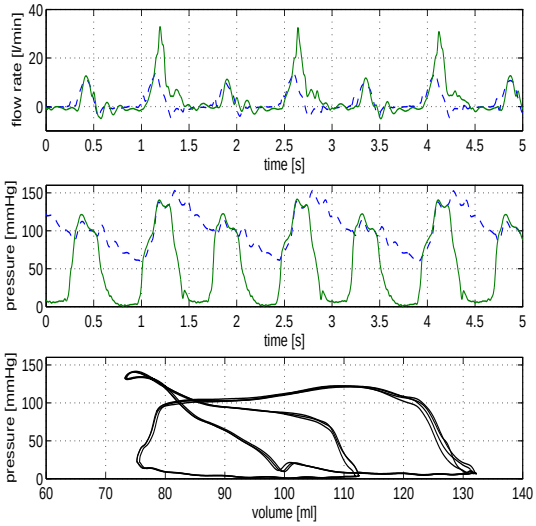

Figure 10: Results of aortic and total flow (upper panel), left-ventricular and aortic pressure (middle panel) and pV loop (lower panel) for LVAD operation.

4 Discussion

A control strategy has been developed that enables a mock circulatory system to reproduce the physiological mechanical functions of the heart, ie. the Frank Starling mechanism. The cardiac function is described by the single fiber model which is capable of adapting its contractile behaviour as a function of time, left ventricular volume and ejection rate. The MCS can operate on a fixed heart rate or adapt its heart rate to changes in systemic pressure by a baroreflex model. Furthermore, the system can be set up to test left ventricular assist devices under a wide variety of conditions, since the single fiber holds several parameters to change the properties of the heart, like speed of contraction and wall volume. A seventh order system of ordinary differential equations was used as a mathematical model for the mock circulatory system to evaluate the control strategy. This model is limited as it simplifies the fluid dynamic behaviour by using a lumped model to describe what is actually a distributed system. However, the model was found to describe the hemodynamics of the system adequately under the conditions studied.

The control strategy is implemented using a pressure feedback control system. A reference left ventricular pressure is calculated by the heart model using left ventricular volume. The servo controller regulates the left ventricular pressure according to this reference signal. The servo controller preserves stability and robustness, and tracks the reference pressure with a bandwidth of 40 Hz. The Nyquist plot in the right panel figure 4 showed that the designed controller is stable and robust with sufficient gain and phase margins. The tracking error is acceptable with an average value of 8%. Although opening and closure of the valves have a major negative effect on the performance, improvements could be made in the future with more accurate data acquisition equipment.

Figure 7 showed that the end-systolic pressure volume ratio (ESPVR) is insensitive to preload changes in both the numerical model and the MCS. These results demonstrated the capability of the control algorithm to mimic preload responses similar to the results obtained in vivo [37]. Changes in afterload showed that ESPVR is linearly dependent on end-systolic volume (figure 8). Increasing the afterload resulted in decreased stroke volume, similar to results obtained in vivo [38]. The ability to reproduce physiological results when loads are significantly changed by the operation of the LVAD is critical for the testing of LVADs in a mock circulatory system.

The shape of the pV loops (figure 7) obtained with the MCS were sufficiently similar to in vivo [37]. However, an increase in volume was observed at the end of the isovolumic relaxation phase caused by the high stiffness of the venous compliance. Furthermore, the closure of the mitral valve caused a deviation at the end of the diastolic phase. The results of figure 8 showed different deviations. A small pressure increase is visible at the isovolumic contraction of the ventricle. This is again caused by the closure of the mitral valve, as the tracking performance is significantly lower at the moment of closing (figure 5).

The left panel of figure 9 showed that the MCS can run on a wide variety of heart rates. The linear relationship for the ESPVR does not hold now, as the variation in rates significantly affects the contraction speed. The ability of the MCS to run on various rates enabled the addition of a baroreflex control model. The baroreflex regulates the heart rate based on systemic pressure. The right panel of figure 9 showed the response of the control algorithm to an increase

in preload in terms of pressure, volume and frequency. The pressure in the left ventricle and the end-diastolic volume both increased, similar to the results of figure 7. The increase in preload caused an instantaneous increase in left-ventricle pressure and hence systemic pressure. The baroreflex mechanism responded by lowering the heart rate, thereby lowering the systemic pressure again.
Figure 10 showed the ability of the mock circulatory system to add a LVAD to its system. Remarkable is the fact that the LVAD is activated once every two heartbeats. This event is also visible in the results of the experiments, as the pV-loop is actually composed of two loops. The loop with higher left-ventricle pressure is formed when the LVAD ejects. The results showed that the MCS responds stable and robust to the introduction of a LVAD.
The deviations in the pV loops of figure (7) and (8) could be eliminated by using a venous compliance with a lower stiffness. It prevents the increase in volume at the end of the isovolumic relaxation and reduces the effect of the closure of the mitral valve. Another limitation of the circulatory system is the fact that it only describes the left part of the heart. The flow from the afterload is directly returned to the preload, which may lead to a too strong coupling. A higher systemic pressure will yield more liquid storage in the afterload. Because of the constant amount of liquid in the circulation, the preload will be automatically lowered, hence reducing the level of filling and thus the cardiac output. The addition of a right circulation could overcome this problem.

5 Conclusion

A new control strategy for a (MCS) has been developed with a cardiac function which is capable of adapting its contractile behaviour as a function of time, and a baroreflex response to mimic the pressure-dependency of the heart rate. A reference left ventricular pressure is calculated by the heart model using left ventricular volume. The left ventricular pressure is regulated by a feedback controller according to this reference signal.
Simulations and experiments on the MCS showed that the system responds to changes in afterload, preload and heart rate stable, robust and consistent with physiological observations. Furthermore, the system can be set up to test left ventricular assist devices under a wide variety of conditions, as the heart model holds several parameters to change the properties of the heart. Future development of the mock circulatory system would benefit from adding a right circulation.

References

1. Arts T, Bovendeerd PHM, Prinzen FW, and Reneman RS. Relation between left ventricular cavitypressure and volume and systolic fiber stress and strain in the wall. Biophys J, 59:93–103, 1991.

2. American Heart Association. Heart disease and stroke statistics 2006 update. Circulation, 113(6):85–151, 2006.

3. Hosenpud JD, Bennett LE, Keck BM, Boucek MM, and Novick RJ. The

registry of the international society for heart and lung transplantation: Seventeenth official report. J Heart Lung Transplant, 19:909–931, 2000.

4. Rose EA, Gelijns AC, Moskowitz AJ, Heitjan DF, Stevenson LW, Dembitsky W, Long JW, Ascheim DD, Tierney AR, Levitan RG, Watson JT, Meier P, Ronan NS, Shapiro PA, Lazar RM, Miller LW, Gupta L, Frazier OH, Desvigne-Nickens P, Oz MC, and Poirier VL. Long-term use of a left ventricular assist device for end-stage heart failure. N Engl J Med, 345:1435–1443, 2001.

5. Westaby S, Katsumata T, Houel R, Evans R, Pigott D, Frazier OH, and Jarvik R. Jarvik 2000 heart: Potential for bridge to myocyte recovery. Circulation, 98:1568–1574, 1998.

6. McCarthy PM, Smedira NO, Vargo RL, Goormastic M, Hobbs RE, Starling RC, and Young JB. Cardiopulmonary support and physiology: one hundred patients with the heartmate left ventricular assist device: evolving concepts and technology. J Thorac Cardiovasc Surg, 115:904–912, 1998.

7. Donovan FM. Design of a hydraulic analog of the circulatory system for evaluating artificial hearts. Biomat Med Devices Artif Organs, 3(4):439–449, 1975.

8. Liu Y, Allaire P, Wood H, and Olsen D. Design and initial testing of a mock human circulatory loop for left ventricular assist device performance testing. Artif Organs, 29:341–345, 2005.

9. Vandenberghe S, Segers P, Meyns B, and Verdonck P. Hydrodynamic characterisation of ventricular assist devices. Int J Artif Organs, 24:470–477, 2001.

10. Helal HA, Watts KC, and Marble AE. Hydrodynamic simulation of arterial networks which include compliant and rigid grafts. J Biomech, 27(3):277–287, 1994.

11. Schima H, Tsangaris S, Zilla P, Kadletz M, and Wolner E. Mechanical simulation of shear stress on the walls of peripheral arteries. J Biomechanics, 23(8):845–851, 1990.

12. Pantalos G, Koenig S, Gillars K, Girdharan G, and Ewert D. Characterization of an adult mock circulation or testing cardiac support devices. ASAIO J, 50:37–46, 2004.

13. Timms D, Hayne M, McNeil K, and Galbraith A. A complete mock circulation loop for the evaluation of left, right and biventricular assist devices. Artif Organs, 29(7):564–572, 2005.

14. Gwak KW, Ricci M, Snyder S, Paden BE, Boston JB, Simaan MA, and Antaki JF. In vitro evaluation of multiobjective hemodynamic control of a heart-assist pump. ASAIO J, 51(4):329–335, 2005.

15. Suga H and Sagawa K. Instantaneous pressure-volume realtionships and their ratio in the excised, supported canine left ventricle. Circ Res, 35:117–126, 1974.

16. Ferrari G, De Lazzari C, Mimmo R, Ambrosi D, and Tosti G. Mock circulatory system for in vitro reproduction of the left ventricle, the arterial tree and their interaction with a left ventricular assist device. J Med Eng Technol, 18(3):87–95, 1994.

17. Ferrari G, De Lazzari C, Mimmo R, Tosti G, Ambrosi D, and Gorczynska K. A computer controlled mock circulatory system for mono- and biventricular assist device testing. Int J Artif Organs, 21(1):26–36, 1998.

18. Ferrari G, Kozarski M, De Lazzari C, Clemente F, Merolli M, Tosti G, Guaragno M, Mimmo R, Ambrosi D, and Glapinski J. A hybrid (numerical-physical) model of the left ventricle. Int J Artif Organs, 24(7):456–462, 2001.

19. Ferrari G, De Lazzari C, Kozarski M, Clemente F, Gorczynska K, Mimmo R, Monnanni E, Tosti G, and Guaragno M. A hybrid mock circulatory system: testing a prototype under physiologic and pathological conditions. ASAIO J, 48:487–494, 2002.

20. Kozarski M, Ferrari G, Clemnte F, Gorczynska K, De Lazzari C, Darowski M, Mimmo R, Tosti G, and Guargagno M. A hybrid mock circulatory system: Development and testing of an electro-hydraulic impedance simulator. Int J Artif Organs, 26(1):53–63, 2003.

21. Ferrari G, Kozarski M, de Lazzari C, Górczyńska K, Tosti G, and Darowski M. Development of a hybrid (numerical-hydraulic) circulatory model: Prototype testing and its response to iabp assistance. Int J Artif Organs, 28(7):750–759, 2005.

22. Baloa LA, Boston JR, and Antaki JF. Elastance-based control of a mock circulatory system. Ann of Biomed Eng, 29:244–251, 2001.

23. Colacino FM, Arabia M, Danieli GA, Moscato F, Nicosia S, Piedimonte F, Valigi P, and Pagnotelli S. Hybrid test bench for evaluation of any device related to mechanical cardiac assistance. Int J Artif Organs, 28(8):817–826, 2005.

24. Vandenberghe S, Segers P, Steendijk P, Meyns B, Dion RAE, Antaki JF, and Verdonck P. Modeling ventricular function during cardiac assist: Does time-varying elastance work? ASAIO J, pages 4–8, 2006.

25. Suga H, Sagawa K, and Demer L. Determinants of instantaneous pressure in canine left ventricle. time and volume specifiaction. Circulation Research, 46:256–263, 1980.

26. Hill AV. The transformation of energy and mechanical work of muscles. Proc Physiol Soc, 51:93–103, 1939.

27. Guyton AC and Hall JE. Textbook of Medical Physiology. W.B. Saunders Company, 9 edition, 1996.

28. van Roon AM, Mulder LJM, Althaus M, and Mulder G. Introducing a baroreflex model for studying cardiovascular effects of mental workload. Psychophysiology, 41:961–981, 2004.

29. Geven MCF, Bohté CN, Aarnoudse WH, van den Berg PMJ, Rutten MCM, Pijls NHJ, and van de Vosse FN. A physiologically representative in vitro model of the coronary circulation. Physiol Meas, 25:891–904, 2004.

30. Franklin GF, Powell JD, and Emami-Naeini A. Feedback control of dynamic systems. Prentice Hall, 4 edition, 2002.

31. Stergiopulos N, Westerhof BE, and Westerhof N. Total arterial inertance as the fourth element of the windkessel model. Am J Physiol, 276:81–88, 1999.

32. Arts T, Delhaas T, Bovendeerd P, Verbeek X, and Prinzen FW. Adaptation to mechanical load determines the shape and properties of heart and circulation: the circadapt model. Am J Physiol, 288:1943–1954, 2005.

33. Kentish JC, ter Keurs HE, Ricciardia L, Bucx JJ, and Noble MI. Comparison between the sarcomere length-force relations of the intact and skinned trabeculae from rat right ventricle. influence of calcium concentrations on these relations. Circ Res, 58:755–768, 1986.

34. Janssen PM and Hunter WC. Force, not sarcomere length, correlates with prolongation of isosarcometric contration. Am J Physiol, 269:676–685, 1995.

35. van Gerven LHM, Rutten MCM, van de Molengraft MJG, Bovendeerd PHM, and van de Vosse FN. Mimicking physiological cardiac function in an in-vitro set-up for testing heart valve. Proc Bioeng Conf, Vail Colorado, United States, June 2005.

36. van de Molengraft MJG, Steinbuch M, and de Kraker A. Integrating experimentation into control courses at the technische universiteit eindhoven. IEEE Control Systems Magazine, 25:40–44, 2005.

37. Maughan WL, Sunagawa K, Burkhoff D, and Sagawa K. Effect of arterial impedance changes ond the end-systolic pressure-volume relation. Circ Res, 54:595–602, 1984.

38. Suga H and Yamakoshi K. Effects of stroke volume and velocity of ejection on end-systolic pressure of left-ventricle. Circ Res, 40:445–450, 1977.

39. Parker TS and Chua LO. Practical numerical algorithms for chaotic systems. Springer-Verlag, Berlin, 1989.

40. Leine RI, van Campen DH, and de Kraker A. Stick-slip vibrations induced by alternate friction models. Nonlin Dyn, 16:41–54, 1998.

A Anatomy and physiology of the heart

The heart is a hollow muscular organ that pumps blood through the vascular system for transport of oxygen and nutrients to the tissue and metabolic waste from the tissue. The heart consists of two pumps, the right and left heart (figure 11). Both sides contain an atrium and a ventricle. The atria collect blood that returns to the heart and facilitate rapid filling of the ventricles. The ventricles pump blood through either the pulmonary (right ventricle) or the systemic circulation (left ventricle). The wall of the right ventricle is thinner and less powerful than the left ventricle. The mitral valve prevents back flow of blood into the left atrium when the left ventricle contracts, and blood is ejected through the aortic valve. The aortic valve prevents back flow of blood from the aorta into the left ventricle. The tricuspid valve prevents back flow of blood into the right atrium when the right ventricle contracts, and blood is ejected through the pulmonary valve. The pulmonary valve prevents back flow from the pulmonary artery to the right ventricle. The outer surface of the heart is called the epicardium and the surface of the cavities is called the endocardium.

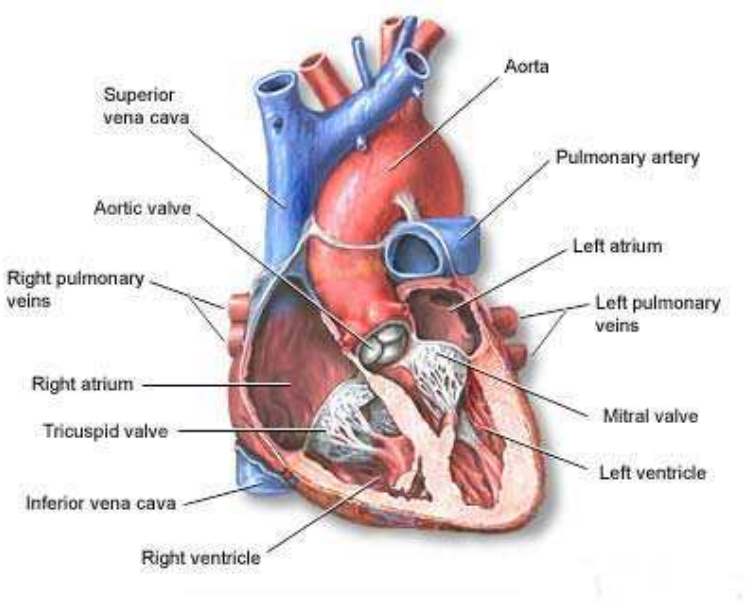

Figure 11: The structure of the heart [27]

The cardiac tissue consists of myofibers which contain sarcomeres, the basic contractile unit of cardiac muscle. Contraction of the sarcomeres results in generation of active stress and myofiber shortening, which translates into ventricular pressure increase and volume decrease.
The cardiac cycle can be divided into four individual phases [27]. In the first, the filling phase, relaxation of the heart muscle enables the ventricles to be filled with blood from the atria. During the isovolumic contraction phase, the ventricles start to contract without volume changes. The pressure in the ventricles starts to rise until the ventricles have built up sufficient pressure to push the

valve open against the pressure in the aorta or pulmonary artery. Opening of the valves marks the beginning of the ejection phase during which blood pours out of the ventricles. As soon as the flow tends to become negative, the aortic or pulmonary valve closes and the isovolumic relaxation phase begins. The period of relaxation (isovolumic relaxation and filling phase) is called diastole, the period of contraction (isovolumic contraction and ejection phase) is called systole.

B Mathematical model

A schematic representation of the setup is shown in figure 12. The mathematic description of the setup is divided into three parts. The hemodynamic preload and afterload are described with a lumped-parameter model. The aortic and mitral valves are described as short tubes in which flow dominated by inertia. The piston pump is described as a mass with friction.

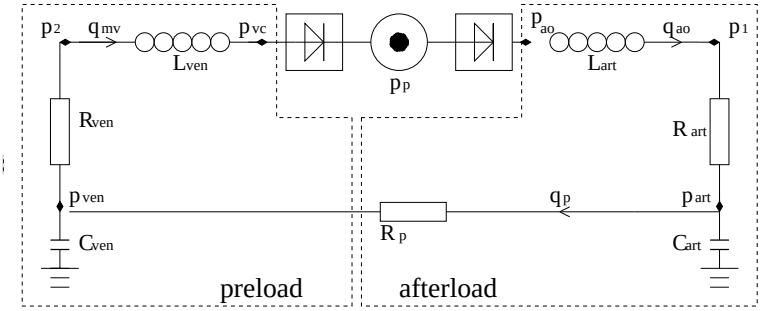

Figure 12: Schematic representation of the systemic circulation

B.1 Hemodynamic preload and afterload

The hemodynamic preload and afterload are described with a lumped parameter model [31]. The whole systemic circulation is described by seven elements. The basic hemodynamic elements used in these models are inertance, resistance and compliance. The inertance and resistance describe the relation between pressure drop and flow. The compliance accounts for the change in volume with pressure. The small arteries and arterioles mainly determine the peripheral resistance. The total arterial compliance accounts for the elasticity of all arteries, with a major contribution from the large vessels. The arterial inertance represents the total inertia in the arteries. The characteristic impedance, modelled as a resistance, describes the combined effect of inertance and compliance in the aorta.

$$\frac{\partial p_1}{\partial t} = R_{art}\frac{\partial q_{ao}}{\partial t} + \frac{\partial p_{art}}{\partial t}, \tag{24}$$

$$\frac{\partial p_2}{\partial t} = -R_{ven}\frac{\partial q_{mv}}{\partial t} + \frac{\partial p_{ven}}{\partial t}, \tag{25}$$

$$\frac{\partial p_{art}}{\partial t} = \frac{1}{C_{art}}q_{ao} + \frac{1}{C_{art}R_p}(p_{ven} - p_{art}), \tag{26}$$

$$\frac{\partial p_{ven}}{\partial t} = -\frac{1}{C_{ven}} q_{mv} + \frac{1}{C_{art} R_p}(p_{art} - p_{ven}). \tag{27}$$

The relations for the aortic pressure p_{ao} and vena cava pressure p_{vc} are:

$$p_{ao} = p_1 + L_{art}\frac{\partial q_{ao}}{\partial t}, \tag{28}$$

$$p_{vc} = p_2 + L_{ven}\frac{\partial q_{mv}}{\partial t}. \tag{29}$$

The values of the parameters are listed in table 2.

B.2 Cardiac Valves

The valves are modelled as short tubes with length l in which flow is dominated by inertia. Conservation of momentum for 1-D problems and incompressible fluids gives

$$\rho(\frac{\partial u}{\partial t} + u\frac{\partial u}{\partial x}) = -\frac{\partial p}{\partial x} \tag{30}$$

with the mediums density ρ, the average velocity over the cross-sectional area u and the pressure in the tube p. Integrating over the tubes length l yields.

$$\Delta p = \frac{1}{2}\rho u^2 + \rho l\frac{\partial u}{\partial t}. \tag{31}$$

Substituting the fluids velocity u with q/A, with flow q and cross-sectional areaA gives a relation between flow q and pressure drop Δp.

$$\frac{\partial q}{\partial t} = \frac{1}{\rho l}\left(\Delta p A - \frac{\rho q^2}{2A}\right) \tag{32}$$

Opening and closing of the valves are modelled by changing the cross-sectional area A of the tube. The valve allows blood to flow only in one direction. This is modelled by assuming that the valve area A depends on the pressure difference and flow direction

$$A = c \cdot A_{open} + (1 - c) \cdot A_{leak} \tag{33}$$

$$c = \begin{cases} 0 & q < 0 \text{ or } \Delta p < 0 \\ 1 & q > 0 \text{ or } \Delta p > 0 \end{cases} \tag{34}$$

with leak area A_{leak} to prevent singularities in the set of equations during closure of the valves. The values of the parameters are listed in table 2.

B.3 Piston pump

The piston pump from the setup is modelled as a closed volume with two valves. The pump is considered as a pressure-source, generating a pressure p_{lv} depending on the piston position and the two flows q_{mv} and q_{av}. The pump also holds a small compliance C_p. The relation for the pressure p_{lv} is shown in (35).

$$\frac{\partial p_{lv}}{\partial t} = \frac{1}{C_p} q_p = \frac{1}{C_p}\left(A_z v + q_{mv} - q_{av}\right) \tag{35}$$

The piston itself is modelled with a second order differential equation

$$\dot{v} + \frac{d}{m}\dot{x} = \frac{1}{m}u(t), \tag{36}$$

with piston mass m and damping d for the friction between the piston and the pump house. The values of the parameters are listed in table 2.

Table 2: Table of the measured and estimated parameters

Symbol	Value	Units			
L_{art}	$3.14 \cdot 10^5$	$Pa \cdot s^2 \cdot m^{-3}$	d	0.4	$kg \cdot s_{-1}$
C_{art}	$1.90 \cdot 10^{-8}$	$m^3 \cdot Pa^{-1}$	L_0	0.045	m
R_{art}	$1.95 \cdot 10^8$	$Pa \cdot s \cdot m^{-3}$	l_{av}	$2.1 \cdot 10^{-2}$	m
R_p	$2.52 \cdot 10^7$	$Pa \cdot s \cdot m^{-3}$	l_{mv}	$2.7 \cdot 10^{-2}$	m
L_{ven}	$7.03 \cdot 10^3$	$Pa \cdot s^2 \cdot m^{-3}$	$A_{open,av}$	$4.5 \cdot 10^{-4}$	m^2
C_{ven}	$3.15 \cdot 10^{-5}$	$m^3 \cdot Pa^{-1}$	$A_{leak,av}$	$4.5 \cdot 10^{-8}$	m^2
R_{ven}	$3.73 \cdot 10^6$	$Pa \cdot s \cdot m^{-3}$	$A_{open,mv}$	$7.2 \cdot 10^{-4}$	m^2
C_p	$1.77 \cdot 10^{-10}$	$m^3 \cdot Pa^{-1}$	$A_{leak,mv}$	$7.2 \cdot 10^{-8}$	m^2
A_z	$2.28 \cdot 10^{-3}$	m^2	ρ	$1.05 \cdot 10^3$	$kg \cdot m{-}3$
m	0.12	kg			

C Single Fiber Model

Arts et al. [1] derived a relation between the cavity pressure and volume and the myocardial fiber stress and strain. This relationship assumes that muscle fiber stress and strain are homogeneously distributed in the normal left ventricle. Fiber stress and strain may be approximated by single values, valid for the whole wall. The myocardial mechanical properties are discussed in the next part. In the last part, these constitutive properties are combined with cardiac geometrical properties, to arrive at the single fiber model.

C.1 Myocardial mechanical properties

Myofiber stress σ_f is a function of sarcomere length l_s and time. The myofiber stress σ_f is modelled with a Hill-type model [26]. The model describes the uniaxial behaviour of a muscle. This model consists of a passive elastic component PE in parallel with a contractile element CE (figure 13. The passive elastic component describes the behaviour of the passive muscle. The contractile element describes the additional stress due to muscle activation, shortening the sarcomere during contraction. The active stress depends on sarcomere length l_s, sarcomere shortening velocity v_s and time t. The fiber stress is a summation of passive stress σ_{pas} and active stress σ_{act}.

$$\sigma_f = \sigma_{pas}(l_s) + \sigma_{act}(l_s, l_{ce}, t), \tag{37}$$

$$\tag{38}$$

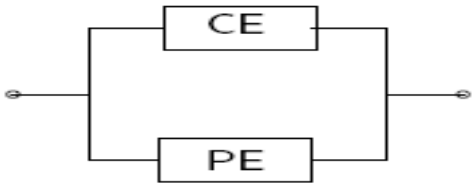

Figure 13: Hill type model suitable for describing myocardial tissue, consisting of a passive element PE and a contractile element CE

C.1.1 Passive material behaviour

The passive stress is described by:

$$\sigma_{pas} = \sigma_{pas0}\exp(c_p(l_s - l_{sp0}) - 1), \tag{39}$$

relating passive axial stress s_{pas} to sarcomere length l_s.

C.1.2 Active material behaviour

The contractile element describes the generation of active stress σ_{act} by the sarcomeres. It is modelled as a function of sarcomere length l_s, time elapsed since activation t_a and sarcomere shortening velocity v_s

$$\sigma_{act}(l_s, t_a, v_s) = f(l_s)g(t_a)h(v_s). \tag{40}$$

The length dependence is modelled according to Kentish et al. [33]

$$f(l_s) = \begin{cases} 0 & l_s \leq l_{sa0} \\ \sigma_{ao}\left(\frac{l_s}{l_{sa0}} - 1\right)^c & l_s > l_{sa0} \end{cases} \tag{41}$$

with σ_{a0} determining the stress level, the parameter l_{sa0} representing the sarcomere length below which active stress development is impossible, and the parameter c describes the curvature of the relation.
The equation for the time-dependence approximates experimental data by Janssen et al. [34]

$$g(t_{t_a}) = \begin{cases} 0 & t_a < 0 \\ sin^2\left(\frac{\pi}{2}\frac{t_a}{\tau_r} - 1\right) & 0 \leq t_a \leq \tau_r \\ 1 - sin^2\left(\frac{\pi}{2}\frac{t_a - \tau_r}{\tau_d} - 1\right) & \tau_r \leq t_a \leq \tau_d + \tau_r \\ 0 & t_a > \tau_r + \tau_d \end{cases} \tag{42}$$

$$\tau_r = \tau_{r0}(a + a_r(l_s - l_{a0})) \tag{43}$$

$$\tau_d = \tau_{d0}(a + a_d(l_s - l_{a0})) \tag{44}$$

with time elapsed since the moment of activation t_a. The rise and decay time of the myofiber are described by τ_r and τ_d. The time constants equal τ_{r0} and τ_{d0} at $l_s = l_{sa0}$. The change of the constants with sarcomere length is governed by parameters a_r and a_d.

The shortening velocity is modelled hyperbolically

$$h(v_s) = \frac{1-(v_s/v_0)}{1+a(v_s/v_0)} \tag{45}$$

and

$$v_s(t) = -\frac{dl_s(t)}{dt}, \tag{46}$$

where v_0 represents the unloaded shortening velocity and a governs the curvature of the hyperbolic relation. The parameters for the single fiber model are derived from literature [33, 34] and shown in table 3.

Table 3: Table of the measured and estimated parameters

Symbol	Value	Units
σ_{a0}	$180 \cdot 10^3$	Pa
c	1.0	-
l_{sa0}	$1.6 \cdot 10^{-6}$	m
τ_{r0}	$50 \cdot 10^{-3}$	s
a_r	$150 \cdot 10^3$	$s \cdot m^{-1}$
τ_{d0}	$100 \cdot 10^{-3}$	s
a_d	$300 \cdot 10^3$	$s \cdot m^{-1}$
v_0	$0.01 \cdot 10^{-3}$	$m \cdot s^{-1}$
a	2.0	-
σ_{p0}	$0.9 \cdot 10^3$	Pa
c_p	$6 \cdot 10^6$	m^{-1}
l_{sp0}	$2.0 \cdot 10^{-6}$	m
V_w	$200 \cdot 10^{-6}$	m^3
V_{lv0}	$66.7 \cdot 10^{-6}$	m^3
l_{s0}	$2.0 \cdot 10^{-6}$	m

C.2 Relation between pump work and myofiber mechanics

Pump work is generated by the summed action of all cardiomyocytes, arranged in a specific structure of myofiber orientations. Local myofiber work is quantified by stress and strain as a function of time. In the model of Arts et al. [1] it is assumed that myofiber stress and strain are homogeneously distributed, so that those values are uniform for the whole ventricular wall.
The myocardial material is considered to be a soft incompressible material embedding myocardial fibers. A fluid fiber model can describe the myocardial tissue, since the mechanical load is transmitted mostly along those fibers [1]. Total Cauchy stress σ_{tot} is determined by intramyocardial pressure p_{im} and fiber stress σ_f

$$\sigma_{tot} = -p_{im}I + \sigma_f \vec{e_f}\vec{e_f}, \tag{47}$$

with $\vec{e_f}$ for the fiber direction. For the stress components in longitudinal, circumferential and radial direction, it holds [1]:

$$\sigma_{ll} = -p_{im} + \sigma_f sin^2\alpha$$

$$\begin{aligned}\sigma_{cc} &= -p_{im} + \sigma_f cos^2\alpha \\ \sigma_{rr} &= -p_{im}\alpha. \end{aligned} \tag{48}$$

The stress in the wall satisfies the equilibrium equation:

$$\vec{\nabla} \cdot \sigma = \vec{0}. \tag{49}$$

When considering a thick walled sphere as the model geometry, the radial component of equation (49) yields:

$$\frac{\partial \sigma_{rr}}{\partial r} + \frac{2\sigma_{rr}}{r} - \frac{1}{r}(\sigma_{ll} + \sigma_{cc}) = 0. \tag{50}$$

Substitution of equation (48) in (50) yields:

$$\frac{\partial \sigma_{rr}}{\partial r} - \frac{1}{r}\sigma_f = 0. \tag{51}$$

This equation describes how the fiber stress contributes to the variation of the radial stress σ_{rr}. The stress difference between inner and outer ventricular-wall $\Delta\sigma_{rr}$ is given by

$$\begin{aligned}\Delta\sigma_{rr} &= \int_{r_i}^{r_o} d\sigma_{rr} \\ \Delta\sigma_{rr} &= \int_{r_i}^{r_o} \frac{\sigma_f}{r} dr \\ \Delta\sigma_{rr} &= \sigma_f ln \frac{r_o}{r_i} \\ \Delta\sigma_{rr} &= \sigma_{rr,r_o} - \sigma_{rr,r_i}. \end{aligned} \tag{52}$$

In the integral, σ_f is taken constant across the wall based on the assumption of homogeneity. Further, the radial wall stress is zero at the epicardial surface ($r = r_o$) and equals minus left ventricular pressure at the inner surface ($r = r_i$). As a result, the pressure difference $\Delta\sigma_{rr}$ is equal to the left ventricular pressure. Rewriting r_o and r_i in terms of ventricular volume V_{lv} and wall volume V_w yields the relation

$$p_{lv} = \frac{1}{3}\sigma_f ln\left(1 + \frac{V_w}{V_{lv}}\right). \tag{53}$$

This relation can be approximated in the physiological range, within an $\pm 5\%$ error (Arts et al. [1])

$$\frac{\sigma_f}{p_{lv}} = \left(1 + 3\frac{V_{lv}}{V_w}\right) \tag{54}$$

Conservation of energy yields a relation between ventricular volume and sarcomere length, with incremental pump work equal to the incremental work generated by the myofibers

$$p_{lv} dV_{lv} = V_w \frac{\sigma_f}{l_s} dl_s. \tag{55}$$

Combining (54) and (55) yields

$$\frac{l_s}{l_{s0}} = \left(\frac{1 + 3\frac{V_{lv}}{V_w}}{1 + 3\frac{V_{lv0}}{V_w}}\right)^{\frac{1}{3}}, \tag{56}$$

where l_{s0} is the sarcomere length in the reference state, and the same holds for the cavity volume V_{lv0}.

D Determination of pump Compliance

The pump in the setup has a compliance, and relates changes in pressure to changes in volume. This parameter is relevant for use in the mathematical model and for calculation of the mitral flow q_{mv}.
The compliance of the pump is estimated with measurements on the pump. The pump housing is completely filled with water and sealed prior to the measurements. The piston is held on a fixed position using a simple lead controller. Changes in volume V_p and pressure p_p, actuated with a random disturbance. Pump pressure and piston position are measured while the piston is actuated. Fourier transformation on the measured signals yields a frequency response function $H = \frac{\partial p}{\partial V}$. The experiment is carried out almost maximum volume, at half the volume and almost minimum volume. Figure 14 shows the frequency responses and their coherence functions. All figures show an almost constant magnitude for low frequencies, the working area of the mock circulatory system. The compliance is assumed to have a constant value of $C_p = 1.77 \cdot 10^{-10}$.

E Controller design

A common method in linear control theory for the design of a servo controller, is manual loop shaping of the open loop frequency response function (FRF) of the system [30]. An advantage of using frequency response functions is the ease with which experimental data can be used for the design of a servo controller. A FRF measurement of the system has been acquired with the sensitivity method, the most common method for FRF measurements in closed loop. This method measures the input voltage to the system u(t) and the excited extra input w(t) to determine an estimation of the sensitivity function $S(\jmath\omega)$ (figure 15). The coherence is plotted for a good measurement quality indication. The coherence function of the sensitivity function shows poor quality ($\ll 1$) for low frequencies due to uncertain nonlinearities such a coulomb and viscous friction. The transfer function $H(\jmath\omega)$ yields from the sensitivity function (figure 15, right).

$$S(\jmath\omega) = \frac{1}{1 + C(\jmath\omega)H(\jmath\omega)} \tag{57}$$

$$H(\jmath\omega) = \frac{1 - S(\jmath\omega)}{C(\jmath\omega)S(\jmath\omega)} \tag{58}$$

The open loop frequency response shows high frequencies noise. This can be explained to the fact that the magnitude is fluctuating between its encoder accuracy due to analog to digital conversion. Another reason for this high frequency noise is the fact that the sensitivity approaches one for high frequencies (figure 15). Thus, the transfer function estimation approaches zero in this area. Little disturbance in the frequency response measurement of the sensitivity function, causes relative large fluctuations in the transfer function estimation.
A integral action is used for disturbance rejection at low frequencies.

$$C_{int}(s) = \frac{s + 2\pi f_i}{s} \tag{59}$$

Enlarging the gain of controller at low frequencies may result in unstable behaviour. Even if the closed loop system is stable, the robustness will be sig-

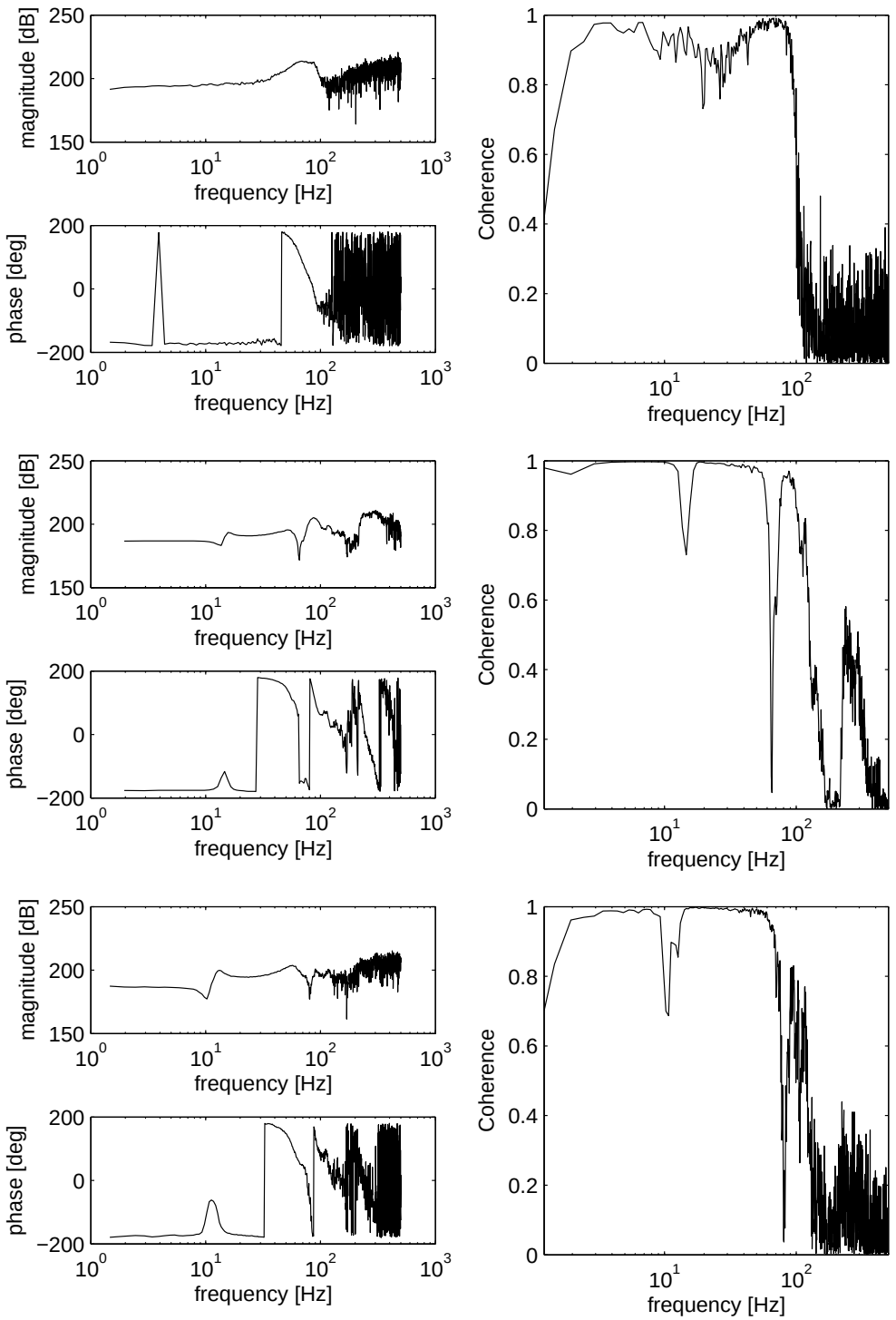

Figure 14: Bode diagram of the frequency response function with no air added to the pump housing. Right figure is the coherence function of the frequency response function.

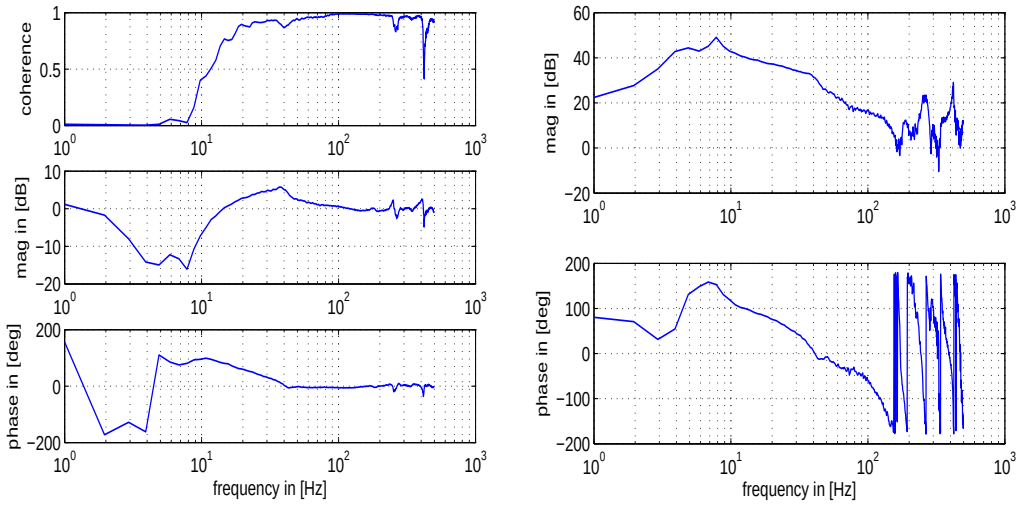

Figure 15: Left panel: Frequency response measurement of sensitivity function and corresponding coherence function. Right panel: Open loop frequency response.

nificantly lowered, as the gain and phase margins may become to small. A lead filter has been used for the required phase advance in the resonance frequency region to increase the robustness. The lead filter improves the transient response, thereby improving stability and robustness.

$$C_{lead}(s) = K_l \frac{\frac{1}{2\pi f_2}s + 1}{\frac{1}{2\pi f_3}s + 1} \tag{60}$$

with $f_2 < f_3$. A second order low-pass filter takes care of measurement noise reduction and robustness at high frequencies.

$$C_{filter}(s) = \frac{1}{\frac{1}{(2\pi f_4)^2}s^2 + \frac{2\beta}{2\pi f_4} + 1} \tag{61}$$

The frequency response function of the controller is shown in the left panel of figure 16. The open loop frequency response in the right panel of figure 16 with a bandwith of 40 Hz. The left panel of figure 17 shows the sensitivity function. The right panel of figure 17 shows the open loop Nyquist plot, showing stability and robustness.
A feedforward controller has been added to improve the performance of the system. The feedforward controller is based on the inverse of the model described by (1) and (2). The pressure trajectory, generated by the single-fiber model, is used as the input for the feedforward, the output signal is added to the servo controller. The controller now tracks the pressure trajectory (figure 18) with error margins smaller than 22 mmHg and an average value of 3.2 mmHg. These peak errors of 22 mmHg are caused by the closure of the mitral valve. During the rest of the trajectory the error is considerably smaller with values below 10 mmHg.

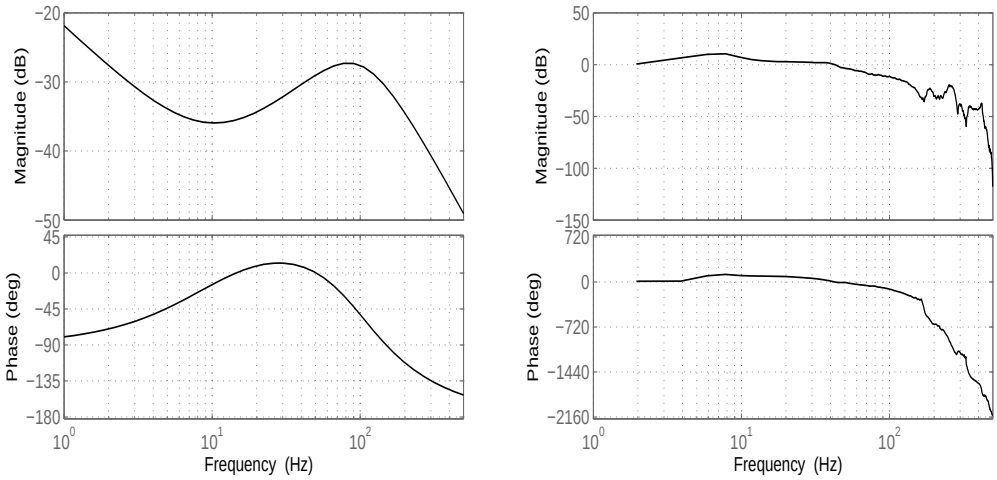

Figure 16: Left panel: Frequency response function of the controller. Right panel: Open loop frequency response.

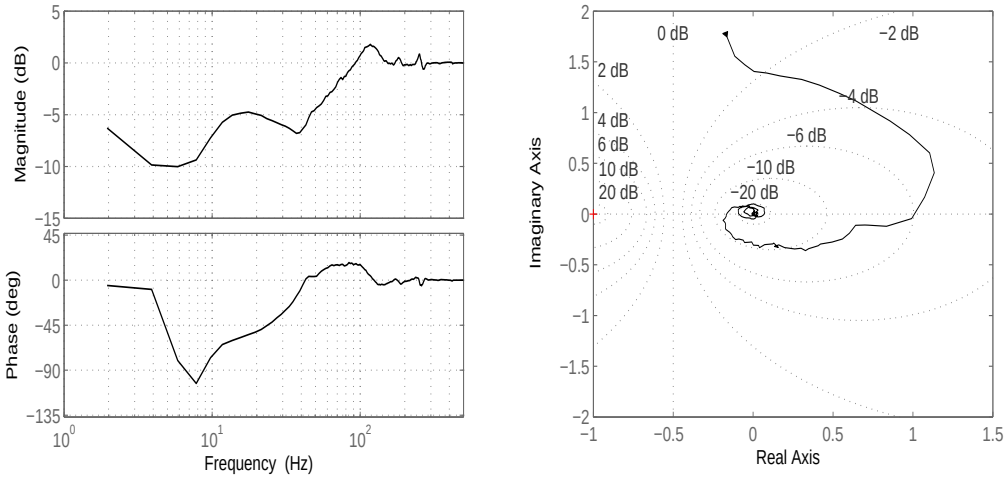

Figure 17: Left panel: Frequency response of the sensitivity function. Right panel: Open loop Nyquist plot.

F Stability Analysis

The system described in this article can be characterized as an non-linear non-autonomous system with a periodic solution. The system is nonlinear due to the nonlinear valve equation. The single-fiber model makes the system non-autonomous and periodic. The periodic solution of the nonlinear system has to

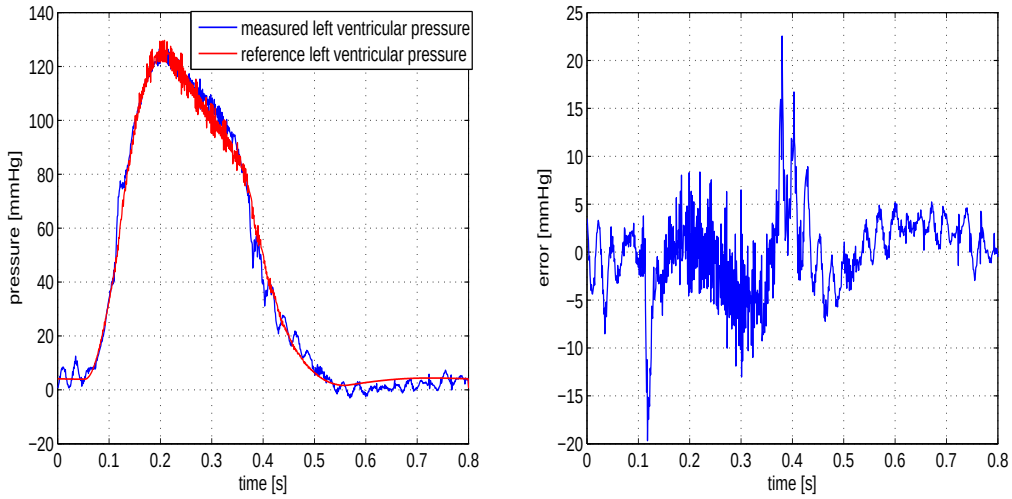

Figure 18: Left panel shows the reference and measured left ventricular pressure. The right panel shows error signal between reference and tracked position signal.

be find in order to study its stability. The stability will be determined for the system without the baroreflex model, because the periodicity will change continuously otherwise. A numerical method, which is called the shooting method, will be used to find the periodic solution [39].

F.1 Nonlinear non-autonomous system

The non-autonomous system from this article can be described by the following set of differential equations

$$\dot{x} = f(x, t), \tag{62}$$

where $\dot{x} = dx/dt$, x is a column with the state variables of the system, t is the time and f is a column of nonlinear function of both x and t. The initial condition is given at $t = t_0$

$$x(t_0) = x_0. \tag{63}$$

The solution to equation (62) after time lapse t_d, satisfying equation (63) is written as $\phi(t, t_0, x_0)$. The system described by (62) has to be extended as our system also contains a periodicity. A periodic non-autonomous system has the additional property

$$f(t, x(t)) = f(t + T, x(t + T)), \quad \forall x \epsilon \tag{64}$$

where T is the period of the system. The periodic solution of a non-autonomous system after time lapse t_d is denoted by $\phi^p(t, t_0, x_0)$.

F.2 Periodic solutions and stability

The system described by equation (62) is linearized around a trajectory $x^p(t) = \rho^p(t, t_0, x_0)$ in order to access the stability properties of the periodic solution. A perturbed solution $x(t) = x^p(t) + \Delta x(t)$ is therefore introduced, satisfying equation (62)

$$\begin{aligned} \dot{x}^p(t) + \Delta\dot{x}(t) &= f(t, x^p(t) + \Delta x(t)) \\ &= f(t, x^p(t)) + \frac{\partial f(t,x)}{\partial x}|x^p(t)\Delta x(t)) + H.O.T., \end{aligned} \tag{65}$$

where H.O.T. stands for higher-order terms. As $\dot{x}^p(t) = f(t, x^p(t))$, the following differential equation for $\Delta x(t)$ remains

$$\Delta\dot{x} = \frac{\partial f(t,x)}{\partial x}|x^p(t)\Delta x(t)) + H.O.T. \tag{66}$$

Since $x^p(t)$ is time-dependent and periodic, $\frac{\partial f(t,x)}{\partial x}|x^p(t)$ is a time-dependent and periodic Jacobian matrix, which will be denoted by $A(t, x^p(t))$

$$\Delta\dot{x} = A(t, x^p(t))\Delta x(t)) + H.O.T.. \tag{67}$$

Linearizing the nonlinear system has led to a Linear (Periodic) Time-Variant (LTV) system (67). To study the stability of the non-autonomous system, the properties of the fundamental solution matrices of LTV systems have to be known.

F.2.1 Linear Time-Varying System

A general linear time-variant (LTV) system can be written as

$$\dot{x}(t) = A(t, x^p(t))x(t) + b(t). \tag{68}$$

Equation (67) becomes after excluding higher order terms

$$\Delta\dot{x}(t) = A(t, x^p(t))\Delta x(t). \tag{69}$$

The perturbation equation (69) is linear time-variant too and has a set of n independent, fundamental solutions $\phi_1(t), \ldots, \phi_n(t)$. The related fundamental solution matrix can be written as

$$\Phi(t, t_0) = [\phi_1(t, t_0) \ldots \phi_n(t, t_0)]. \tag{70}$$

Consequently,

$$\dot{\Phi}(t, t_0) = A(t)\Phi(t, t_0), \quad with \quad \Phi(t_0, t_0) = I. \tag{71}$$

Since, $\Phi(t, t_0)$ contains the fundamental solutions of (69) for specific initial conditions x_0, and the superposition principle with respect to initial conditions holds for the linear equation (69), the perturbed solution can be written as

$$\Delta x(t) = \Phi(t, t_0)\Delta x(t_0) \tag{72}$$

for arbitrary $\Delta x(t_0)$. When $\Delta x(t)$ in equation (69) is considered to be a perturbation around a trajectory of the nonlinear system (62), the fundamental solution matrix relates how an infinitely small perturbation evolves to an infinitely small perturbation after time t.

An important property of the fundamental solution matrix, which is needed later on, can be derived from (72)

$$\begin{aligned} \Delta x(t_1) &= \Phi(t_1, t_0)\Delta x(t_0) \\ \Delta x(t_2) &= \Phi(t_2, t_1)\Delta x(t_1), \end{aligned} \tag{73}$$

for $t_0 \leq t_1 \leq t_2$. Consequently,

$$\Delta x(t_2) = \Phi(t_2, t_1)\Phi(t_1, t_0)\Delta x(t_0) = \Phi(t_2, t_0)\Delta x(t_0) \tag{74}$$

and thus

$$\Phi(t_2, t_0) = \Phi(t_2, t_1)\Phi(t_1, t_0), \tag{75}$$

which is called the transition property of the fundamental solution matrix.

F.2.2 Linear Periodic Time-Variant Systems

In a linear periodic time-variant system A(t) is considered to depend on time in a periodic way: $A(t) = A(t + T)$. Because A(t) is periodic, it follows that

$$\Phi(t, t_0) = \Phi(t + T, t_0 + T) = \Phi(t + kT, t_0 + kT), k = 0, 1, 2, \ldots \tag{76}$$

and

$$\Phi_T = \Phi(t_0 + T, t_0) = \Phi(t_0 + (k + 1)T, t_0 + kT), k = 0, 1, 2, \ldots \tag{77}$$

$\Phi_T = \Phi(t_0 + T, t_0)$ is called the monodromy matrix and is equal to the value of the fundamental solution matrix at $t = t_0 + T$. The monodromy matrix plays an important role in analyzing whether or not the fundamental solution $\Phi(t, t_0)$ matrix grows as time proceeds. Namely, from equation (**??**) follows that $\Delta x(T) = \Phi(t_0 + T, t_0)\Delta x(t_0)$. This equation expresses that $\Phi_T = \Phi(t_0 + T, t_0)$ maps an initial condition $\Delta x(t_0)$ to the response $\Delta x(t_T)$ one period later (figure 19). Combining equation (75), (76) and (77) leads to

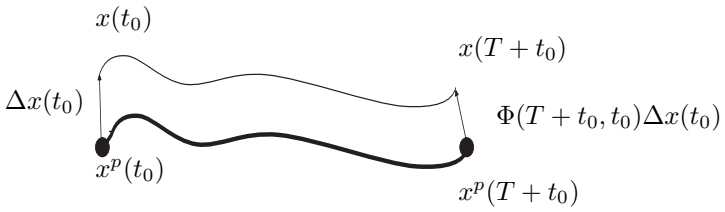

Figure 19: Definition of the monodromy matrix.

$$\Phi(t = 2T, t_0) = \Phi(t + T, t_0)\Phi_T = \Phi(t, t_0)(\Phi_T)^2 \tag{78}$$

and

$$\Phi(t + kT, t_0) = \Phi(t, t_0(\Phi_T)^k, k = 0, 1, 2, \ldots \tag{79}$$

These equations proof again that the monodromy matrix determines the long-term behaviour of the fundamental solution matrix. A consequence of (78) is that the fundamental solution matrix is known for all time t if it is known for

$t_0 \leq t \leq t_0 + T$.
The eigenvalue decomposition of the monodromy matrix is

$$\Phi_T = U\Lambda U^{-1}. \tag{80}$$

Λ is a diagonal matrix with the eigenvalues on the diagonal and U contains the eigencolumns, if the eigenvalues are distinct. Equation (80) can also be written as

$$\Phi_T^k = U\Lambda^k U^{-1}. \tag{81}$$

When applying this equation to (79), it becomes

$$\Phi_{t+kT,t_0} = \Phi(t,t_0)U\Lambda U^{-1}, \quad k = 0,1,2,\ldots. \tag{82}$$

From this equation it can be concluded that the long-term behaviour of the fundamental solution matrix is determined by the eigenvalues λ_i of the monodromy matrix. The eigenvalues are commonly called Floquet multipliers or characteristic multipliers. The growth or decay of a perturbation follows from (72) and (81)

$$\Delta x(t_0 = kT) = U\Lambda^k U^{-1}\Delta x(t_0), k = 0,1,2,\ldots. \tag{83}$$

The Floquet multipliers determine the exponential growth or decay of a perturbation. If $|\lambda_i| > 1$, then a perturbation grows in the direction of its eigenvector. If $|\lambda_i| < 1$, then a perturbation decays in the direction of its eigencolumn. The Floquet multipliers will be used for the stability analysis of the periodic solution of the nonlinear system.

F.3 Stability of Periodic Solutions of Nonlinear Systems

The nonlinear system (66) can be linearized around the periodic solution of the system $x^p(t)$, which leads to a linear time-varying system as in (67). The Floquet multipliers of the LTV system can now be used to analyse the stability of a periodic solution of the nonlinear system. The Floquet multipliers determine the exponential growth or decay of the perturbations in the eigendirections of the monodromy matrix Φ_T and hence the stability of the periodic solution. Although the fundamental solution matrix is dependent on the initial condition $x^p(t_0)$, the Floquet multipliers are not (for proof see [40]). Only the eigendirections will be different. In other words, the choice of initial conditions does not influence the stability analysis, as long as it is on the periodic solution.
The periodic solution of the system $x^p(t)$ is found with the shooting method. This method uses the Newton-Raphson algorithm as zero finding algorithm.

F.3.1 The Newton-Raphson Algorithm

Various numerical algorithms exist for finding periodic solutions. These algorithms are called periodic solution solvers and are based on the formulation of the problem as a zero of a certain function. A zero of this function is found with a zero-finding algorithm, the Newton-Raphson algorithm in this case. The Newton-Raphson algorithm is a commonly used technique for locating zeros of a function. Let the nonlinear function $f(x)$ have a zero at point x^*, that is

$f(x^*) = 0$. The algorithm calculates x^* by iterating from an initial guess $x^{(0)}$ using the relation

$$x^{(i+1)} = x^{(i)} - \frac{f(x^{(i)})}{f'(x^{(i)})}, \tag{84}$$

where i indicates the iteration count. The initial guess should be sufficiently close to the actual zero at point x^* to guarantee convergence. The algorithm (84) is iterated until some convergence criterion is met or is stopped when the method diverges. Most convergence tests check whether the value of $f(x^{(i)})$ approximates zero within a certain tolerance. The iteration scheme is stopped when the scheme is not converging monotonically, $f(x^{(i+1)}) > f(x^{(i)})$, or when a maximum number of iterations is exceeded.

F.3.2 The Shooting Method

The shooting method is an algorithm for finding periodic solutions of the system by solving a two-point boundary value problem, in which solutions are sought of

$$H(x_0) = x_T - x_0 = 0 \tag{85}$$

with the Jacobian

$$DH(x) = \Phi(t_0 + T, x, t_0) - I \tag{86}$$

The zero of equation (85) is solved using the Newton Raphson algorithm (84)

$$(\Phi(t_0 + T, x_0) - I)\Delta x_0 = x_0 - \phi(t_0 + T, t_0, x_0) \tag{87}$$

The following iteration scheme yields from equation (87)

$$[\Phi(t_0 + T, x_0^{(i)}) - I][\Delta x_0^{(i)}] = [x_0^{(i)} - \phi(t_0 + T, x_0^{(i)})] = [x_0^{(i)}] + [\Delta x_0^{(i)}] \tag{88}$$

where i indicates the iteration count. The scheme is reiterated until $H(x_0)$ approximates zero.
The monodromy matrix $\Phi(t_0 + T, x_0)$ is determined by applying a sensitivity analysis [40]. The following relation is used

$$\partial x(t) = \Phi(t, x_0)\partial x_0. \tag{89}$$

One component j of the initial state vector x_0 is perturbed with a small perturbation and the other components remain unaltered

$$\tilde{x}_0^j = x_0 + \partial x_0^j, \tag{90}$$

with

$$\partial x_0^j = [0^1 \cdots 0 \xi^j 0 \cdots 0^n]^T. \tag{91}$$

Where $\xi \ll x_0$ and the superscript j indicates which element in the initial state vector is perturbed. The system is integrated over (period time) T with x_0^j as initial state vector, yielding x_T^j. The perturbation of the initial state vector causes a perturbation of the final state vector.

$$\partial x_T^j = \tilde{x}_T^j - x_T. \tag{92}$$

The elements of the monodromy matrix can be written as

$$\Phi_{i,j}(t_0 + T) = \frac{\partial x_{T_i}^j}{\xi} \tag{93}$$

F.4 Stability of the control strategy

The stability of the complete system has been determined by solving the monodromy matrix Φ_T and determining the eigenvalues of the matrix. The corresponding Floquet multipliers are:

$$\begin{aligned} \lambda_1 &= 0.0 \\ \lambda_2 &= 0.27 \\ \lambda_3 &= 7.2 \cdot 10^{-3} \\ \lambda_4 &= 3.4 \cdot 10^{-3} \\ \lambda_5 &= 3.4 \cdot 10^{-3} \\ \lambda_6 &= 0.4 \cdot 10^{-3} \\ \lambda_7 &= 2.3 \cdot 10^{-6} \\ \lambda_8 &= 1.0 \\ \lambda_9 &= 1.0 \\ \lambda_{10} &= 1.0 \end{aligned} \tag{94}$$

The Floquet multipliers are all within the unit circle, except for three. Those Floquet multipliers are on the unit circle, which means that the periodic solution is marginally stable. As a result, a disturbance applied in the direction of the eigenvector of the corresponding Floquet multiplier will nog vanish nor explode but will stay on the periodic solution. The direction of the eigenvector for all three eigenvalues are in the direction of P_1 and P_{art}.

G List of symbols and subscripts

Symbols

V	m^3	volume
p	Pa	pressure
x	m	piston position
v	$m \cdot s^{-1}$	piston velocity
u	V	input voltage
m	kg	piston mass
d	$kg \cdot s_{-1}$	piston damping
A_z	m^2	piston area
L_0	m	piston length
q	$m^3 \cdot s^{-1}$	flow
C	$m^3 \cdot Pa^{-1}$	compliance
C_p	$m^3 \cdot Pa^{-1}$	pump compliance
R	$Pa \cdot s \cdot m^{-3}$	resistance
R_p	$Pa \cdot s \cdot m^{-3}$	peripheral resistance
L	$Pa \cdot s^2 \cdot m^{-3}$	inertance
ρ	$kg \cdot m^{-3}$	medium density
l	m	valve length
A	m^2	valve area
A_{open}	m^2	area open valve
A_{leak}	m^2	area closed valve
σ_f	Pa	myofiber stress
σ_{pas}	Pa	passive myofiber stress
σ_{act}	Pa	active myofiber stress
σ_{pas0}	Pa	scaling parameter for passive stress
σ_{a0}	Pa	scaling parameter for active stress
l_s	m	sarcomere length
l_{s0}	m	reference sarcomere length
l_{sp0}	m	contraction model parameter
l_{sa0}	m	sarcomere length with zero stress
l_{a0}	m	contraction model parameter
v_s	$m \cdot s^{-1}$	sarcomere shortening velocity
v_0	$m \cdot s^{-1}$	unloaded shortening velocity
t	s	time
t_a	s	time since onset activation
c_p	m^{-1}	contraction model parameter
c	-	curvature of stress-length relation
a	-	curvature of stress-velocity relation
τ_a	s	rise time of the myofiber
τ_d	s	decay time of the myofiber
τ_{r0}	s	rise time active stress for $l_s = l_{a0}$
τ_{d0}	s	decay time active stress for $l_s = l_{a0}$
a_r	$s \cdot m^{-1}$	length dependence of rise time
a_d	$s \cdot m^{-1}$	length dependence of decay time

Symbols (continued)

V_w	m^3	left ventricle wall volume
V_{lv0}	m^3	left ventricular reference cavity volume
$u(t)$	V	input
$w(t)$	V	random uncorrelated noise
$y(t)$	Pa	output
Phi_t	-	monodromy matrix
λ	-	eigenvalue

Subscripts

lv	left ventricular
ao	aortic
art	arterial
ven	venous
vc	vena cava
p	peripheral
z	pump
mv	mitral valve
av	aortic valve
f	fiber
s	sarcomere